

The effect of AGN feedback on the halo mass function

Weiguang Cui^{1,2,3} ^{*}, Stefano Borgani^{3,4,5} & Giuseppe Murante³

¹ *ICRAR, University of Western Australia, 35 Stirling Highway, Crawley, Western Australia 6009, Australia*

² *ARC Centre of Excellence for All-Sky Astrophysics (CAASTRO)*

³ *Astronomy Unit, Department of Physics, University of Trieste, via Tiepolo 11, I-34131 Trieste, Italy*

⁴ *INAF – Astronomical Observatory of Trieste, via Tiepolo 11, I-34131 Trieste, Italy*

⁵ *INFN – Sezione di Trieste, I-34100 Trieste, Italy*

28 February 2024

ABSTRACT

We investigate baryon effects on the halo mass function (HMF), with emphasis on the role played by AGN feedback. Halos are identified with both Friends-of-Friends (FoF) and Spherical Overdensity (SO) algorithms. We embed the standard SO algorithm into a memory-controlled frame program and present the `Python spherIcAl Overdensity` code — `PIAO` (Chinese character: 漂).

For both FoF and SO halos, the effect of AGN feedback is that of suppressing the HMFs to a level even below that of Dark Matter simulations. The ratio between the HMFs in the AGN and in the DM simulations is ~ 0.8 at overdensity $\Delta_c = 500$, a difference that increases at higher overdensity $\Delta_c = 2500$, with no significant redshift and mass dependence. A decrease of the halo masses ratio with respect to the DM case induces the decrease of the HMF in the AGN simulation. The shallower inner density profiles of halos in the AGN simulation witnesses that mass reduction is induced by the sudden displacement of gas induced by thermal AGN feedback. We provide fitting functions to describe halo mass variations at different overdensities, which can recover the HMFs with a residual random scatter $\lesssim 5$ per cent for halo masses larger than $10^{13} h^{-1} M_\odot$.

Key words: cosmology: theory – galaxies: formation

1 INTRODUCTION

The halo mass function (HMF hereafter) is a unique prediction of cosmological models of structure formation. The evolution of the HMF traced by galaxy clusters has been recognized since a long time as a powerful tool to trace the growth of cosmic structures and, therefore, to constrain cosmological parameters (see Rosati et al. 2002; Allen et al. 2011, for reviews, and references therein). In particular, cosmological applications of the HMF require to know its shape and evolution to a high precision, in order to fully exploit its potential as a cosmological tool to be applied to ongoing and future large surveys of galaxy clusters (e.g. Wu et al. 2010; Murray et al. 2013).

N-body simulations covering wide dynamic ranges are nowadays providing rather accurate calibration of the mass function of Dark Matter (DM) halos (e.g. Jenkins et al. 2001; Reed et al. 2003, 2007, 2013; Lukić et al. 2007; Tinker et al. 2008; Crocce et al. 2010; Courtin et al. 2011; Bhattacharya et al. 2011; Angulo et al. 2012; Watson et al. 2013). Various extensions of the standard Λ CDM cos-

mology model, such as coupled dark energy models (e.g. Cui et al. 2012; Baldi 2012), modified gravity models (e.g. Schmidt et al. 2009; Zhang et al. 2013; Puchwein et al. 2013), non-Gaussian initial conditions (e.g. Grossi et al. 2009; Pillepich et al. 2010), massive neutrinos (e.g. Brandbyge et al. 2010; Ichiki & Takada 2012; Costanzi et al. 2013), Warm Dark Matter (e.g. Schneider et al. 2013; Angulo et al. 2013), have been studied using numerical simulations, and their effect on the HMF has been investigated.

A crucial aspect in the calibration of the HMF is related to the algorithm used to identify halos, the two most widely used being the Friend of Friend (FoF) one and the Spherical Overdensity (SO) one. The choice of a specific algorithm clearly impacts both the number of identified halos and their mass (e.g. White 2001, 2002; Lukić et al. 2009; More et al. 2011; Watson et al. 2013, ; see also Knebe et al. 2011 for a detailed comparison between different halo finders).

All the above mentioned HMF calibrations are based on N-body simulations that follow the evolution of a collisionless DM fluid. On the other hand, the presence of baryons is known to add subtle but sizeable effects on halo formation and internal structure, whose details also depend on

^{*} E-mail: weiguang.cui@uwa.edu.au

the physical processes included in the numerical treatment of the baryonic component, such gas cooling, star formation and energy feedback from supernovae (SN) and Active Galactic Nuclei (AGN) (e.g. Kravtsov & Borgani 2012, and references therein).

A number of studies based on cosmological hydrodynamical simulations have been recently carried out to analyse in detail the effect of baryonic processes on different properties of the total mass distribution, such as the power spectrum of matter density fluctuations (Rudd et al. 2008; van Daalen et al. 2011; Casarini et al. 2012, e.g.), the halo correlation functions (e.g. Zhu & Pan 2012; van Daalen et al. 2013), the halo density profiles (e.g. Duffy et al. 2010; Lin et al. 2006) and concentration (e.g. Rasia et al. 2013; Bhattacharya et al. 2013), and the HMF (e.g. Stanek et al. 2009; Cui et al. 2012; Sawala et al. 2013; Martizzi et al. 2013; Cusworth et al. 2013; Balaguera-Antolínez & Porciani 2013; Wu & Huterer 2013).

As for the effect of non-radiative hydrodynamics, the presence of baryons has been shown to induce a slight increase of the HMF (Cui et al. 2012, hereafter Paper I). When extra-heating is included, Stanek et al. (2009) found instead a decrease in the HMF. As for the effect of radiative cooling, star formation and SN feedback, different groups consistently found an increase of the HMF, an effect that is more evident in the high-mass end (Stanek et al. 2009; Cui et al. 2012; Martizzi et al. 2013). On the other hand, Sawala et al. (2013) found that efficient SN feedback produces an opposite effect in low-mass halos.

On the other hand, a number of analyses have shown in the last years that including AGN feedback in cosmological simulations provides populations of galaxy clusters in better keeping with observational results (e.g. Puchwein et al. 2008; Short et al. 2010; Fabjan et al. 2010; McCarthy et al. 2011; Planelles et al. 2013; Le Brun et al. 2013). When the AGN feedback is included, different results were found by Martizzi et al. (2013) and Cusworth et al. (2013). The former showed that the HMF with AGN feedback is higher than the fitting function from Tinker et al. (2008), while the latter predicted a lower HMF compared to the same fitting function. However, their implementation of the AGN feedback differ. Martizzi et al. (2013) described AGN feedback by computing explicitly gas accretion rates onto super-massive black holes (SMBHs) included as sink particles in simulations that also include radiative cooling, star formation and SN feedback (e.g. Springel et al. 2005b; Booth & Schaye 2009). Cusworth et al. (2013) included AGN feedback by computing the associated feedback energy from the semi-analytic model of galaxy formation by Guo et al. (2011), without including radiative cooling and assuming zero mass for gas particles, so that no back-reaction of baryons on the DM distribution is allowed.

In this paper we extend our previous analysis of baryonic effects on the HMF, presented by Paper I, by also including in our simulations the effect of AGN feedback. We directly compare the HMF obtained from DM-only simulations to those produced by radiative hydrodynamical simulations both with and without AGN feedback, using exactly the same initial conditions, mass and force resolutions. The plan of the paper is as follows. In section 2, we present the simulations analysed in this paper. Section 3 is devoted to

the description of the halo identification methods. In section 4 we present the results of our analysis and describe in detail the differences in the HMF induced by different feedback models. Our results are discussed and summarised in Section 5.

2 THE SIMULATIONS

Three large-volume simulations are analysed in this paper, namely two hydrodynamical simulations which include different description of feedback processes affecting the evolution of baryons and one N-body simulation including only DM particles. Initial conditions for these simulations are the same as described in Paper I and we refer to that paper for further details. The hydrodynamical simulations have the same number dark matter particles (1024^3) and gas particles (1024^3). A first hydrodynamical simulation includes radiative cooling, star formation and kinetic SN feedback (CSF hereafter), while the second one also includes the effect of AGN feedback (AGN hereafter). As for the DM simulation, it starts for the same initial conditions as the hydrodynamical simulations, with the gas particles replaced by collisionless particles, so as to have the same description of the initial density and velocity fields as in the hydrodynamical simulations.

The three simulations have been carried out using the TreePM-SPH code GADGET-3, an improved version of the GADGET-2 code (Springel 2005). Gravitational forces have been computed using a Plummer-equivalent softening which is fixed to $\epsilon_{Pl} = 7.5h^{-1}$ physical kpc from $z = 0$ to $z = 2$, and fixed in comoving units at higher redshift. The simulations assume flat Λ CDM cosmology with $\Omega_m = 0.24$ for the matter density parameter, $\Omega_b = 0.0413$ for the baryon contribution, $\sigma_8 = 0.8$ for the power spectrum normalisation, $n_s = 0.96$ for the primordial spectral index, and $h = 0.73$ for the Hubble parameter in units of $100 \text{ km s}^{-1} \text{ Mpc}^{-1}$. Initial conditions have been generated at $z = 49$ using the Zelovich Approximation for a periodic cosmological box with comoving size $L = 410 h^{-1} \text{ Mpc}$. The masses of gas and DM particles have a ratio such that to reproduce the cosmic baryon fraction, with $m_g \simeq 7.36 \times 10^8 h^{-1} M_\odot$ and $m_{DM} \simeq 3.54 \times 10^9 h^{-1} M_\odot$, respectively.

In the hydrodynamical simulations, radiative cooling is computed for non-zero metallicity using the cooling tables by Sutherland & Dopita (1993), also including heating/cooling from a spatially uniform and evolving UV background. Gas particles above a given threshold density are treated as multi-phase, so as to provide a sub-resolution description of the inter-stellar medium, according to the model described by Springel & Hernquist (2003). Conversion of collisional gas particles into collisionless star particles proceeds in a stochastic way, with gas particles spawning a maximum of two generations of star particles. We also include a description of metal production from chemical enrichment contributed by SN-II, SN-Ia and AGB stars, as described by Tornatore et al. (2007). Kinetic feedback is implemented by mimicking galactic ejecta powered by SN explosions, with a wind mass upload proportional to the local star-formation rate, $\dot{M}_w = \eta \dot{M}_*$. In the CSF simulation we use $\eta = 2$ and $v_w = 500 \text{ km s}^{-1}$ for the wind velocity, which corresponds to assuming about unity efficiency for the con-

version of energy released by SN-II into kinetic energy for the adopted Salpeter IMF.

As for the AGN simulation, it includes both the effect of galactic winds, with $v_w = 350 \text{ km s}^{-1}$ and the same mass-load parameter $\eta = 2$, along with energy feedback resulting from gas accretion onto SMBHs. The model of AGN feedback used in this simulation is the same as that adopted by Fabjan et al. (2010) and is largely inspired to the model originally introduced by Springel et al. (2005a). SMBHs, seeded with an initial mass of $10^6 M_\odot$ in halos resolved with at least 100 DM particles, subsequently grow by merging with other BHs and by gas accretion. The latter proceeds at the Bondi rate and is Eddington-limited. A fraction $\epsilon_r = 0.1$ of accreted mass is converted into radiation, with a fraction ϵ_f of this radiation thermally coupled to the surrounding gas. We assume $\epsilon_f = 0.1$ which increases by a factor of four whenever accretion takes place at a rate of at most one-hundredth of the Eddington limit.

We note that the main motivation for efficient SN feedback with $v_w = 500 \text{ km s}^{-1}$ in the CSF simulations lies in the need of reconciling simulation predictions on the cosmic star formation rate with observations, at least at redshift $z > 2$, a choice that still produces too efficient star formation at lower redshift (e.g. Tornatore et al. 2010). Although AGN feedback is motivated by the need of reducing the star formation rate at lower redshift, still its effect is quite significant already at $z \sim 2$. Therefore, in order to prevent too strong a reduction of star formation around this redshift when SN and AGN feedbacks are both included, we decided to reduce by a factor of two the kinetic energy associated to the former. This lowers the resulting wind velocity to $v_w = 350 \text{ km s}^{-1}$.

3 HALO IDENTIFICATION

The two most common methods used for halo identification in simulations are the Friend-of-Friend (FoF) algorithm (e.g. Davis et al. 1985) and the spherical overdensity (SO) algorithm (Lacey & Cole 1994). The FoF algorithm has only one parameter, b , which defines the linking length as bl where $l = n^{-1/3}$ is the mean inter-particle separation, with n the mean particle number density. In the SO algorithm, there is also only one free parameter, namely the overdensity Δ_c . The overdensity determines the aperture of the sphere, within which the total mean density is $\Delta_c \rho_{crit}$. Here, ρ_{crit} is the critical cosmic density. Each of the two halo finders has its own advantages and shortcomings (see more details in Jenkins et al. 2001; White 2001; Tinker et al. 2008, and references thereon), and the differences between the two methods in terms of halo masses and HMFs have been discussed in several analysis (e.g. White 2002; Reed et al. 2003, 2007; Cohn & White 2008; More et al. 2011; Anderhalden & Diemand 2011; Knebe et al. 2013; Watson et al. 2013). We adopt both methods to identify halos in this paper.

3.1 Friend-of-Friend Halos

In our three simulations FoF halos are identified by a on-the-fly FoF finder, with a slight smaller linking length $b = 0.16$ compared to commonly used one, $b = 0.2$. Dark matter

particles are linked first. Then, each gas and star particle is linked to the nearest dark matter particle, whenever the linking criterion is satisfied.

3.2 Spherical Overdensity Halos – PIAO

We carry out a spherical overdensity (SO) halo search by using an efficient memory-controlled parallel Python **spherIcAl Overdensity** halo finding code — PIAO (Chinese character: 漂). This code is based on the standard SO algorithm. Its aim is not to provide a new halo identification method, but to analyse large simulations on a small computer server or PC with limited memories. To overcome a memory deficiency problem, we adopt a simple strategy, which is based on splitting the whole simulation box into small mesh-boxes, and analysing them one-by-one. The details of this strategy and how to incorporate it within the SO method is discussed in Appendix A. PIAO is parallelised with a python MPI package (MPI4py) to speed up the calculation by taking advantage of multi-core CPUs.

We applied PIAO to the three simulations analysed in this paper. For all of them, SO halos are identified at three different overdensity values¹, $\Delta_c = 2500, 500, 200$. As detailed in the appendix, local density maxima around which growing spheres encompassing a given overdensity, are searched by assigning density at the positions of particles using 64 SPH neighbours and without allowing halos to overlap with each other.

3.3 Matching halos

Since all three simulations share the same initial conditions, dark matter particles have the same progressive identification number (IDs). We exploit this information to match halos identified in different simulations. Using a given halo identified in the DM simulation as the reference, a halo in the CSF or AGN simulation is defined to be the counterpart of the DM halo whenever it includes the largest number of DM particles belonging to the latter. We define the matching rate as the ratio of matched to total number of dark matter particles in the DM halo. Clearly, the larger this rate, the more accurate is the matching. In order to avoid multi-matching, i.e. two halos from CSF/AGN simulation matched to one halo in the DM one, only halos with matching rate larger than 0.5 are selected. We verified that the fractions of matched SO halos for $\Delta_c = 500$, are 97.5% at $z = 0$, 98.3% at $z = 0.6$, 98.6% at $z = 1.0$ and 99.4% at $z = 2.2$. Most of the mismatched halos have smaller halo mass, e.g. 85% of them have halo mass $M_{500} < 10^{13} h^{-1} M_\odot$ at $z = 0$.

At each overdensity Δ_c , we only consider halos with $M_{\Delta_c} \geq 10^{12.5} h^{-1} M_\odot$. With this choice, the smallest halo can still have ~ 1000 particles within the corresponding R_{Δ_c} . However, to allow for a complete matching, we consider halos as small as $M_{\Delta_c} = 10^{11.5} h^{-1} M_\odot$ in the AGN and CSF simulations to be matched to the halos in the DM simulation. As shown by Reed et al. (2013), halos resolved with fewer than $N \sim 1000$ particles are unlikely

¹ In the following, the overdensity value Δ_c is expressed in units of the cosmic critical density at a given redshift, $\rho_c(z) = 3H^2(z)/(8\pi G)$.

to be used for a high-accuracy HMF measurement. Furthermore, Watson et al. (2013) also pointed out that the correction for low number of particles sampling FoF halos from Warren et al. (2006) is ~ 2 per cent for the FoF halos containing 1000 particles. We used a fixed mass bin $\Delta \log M = 0.2$ for the calculation of the HMF, without further correction. As discussed by Lukić et al. (2007), the uncertainty in the HMF resulting from the choice of the binning is negligible as long as the bin width does not exceed $\Delta \log M = 0.5$.

4 RESULTS

Basic information on the number of halos identified by the FoF and SO finders can be obtained from the cumulative HMF. We just mention here that over 10^4 halos are always found with both methods at $z = 0$ with halo mass $M \geq 10^{12.5} h^{-1} M_\odot$. This number can reach ~ 70000 for FoF halos and for SO halos with $\Delta_c = 200$. At the highest considered redshift, $z = 2.2$, this number is still $\sim 10^4$ for FoF and for SO halos with $M_{200} \geq 10^{12.5}$. However, at the same redshift we only have $\sim 10^3$ SO halos with $M_{2500} \geq 10^{12.5} h^{-1} M_\odot$. The CSF simulation has more both SO and FoF halos than the DM one at all redshifts and halo masses, an increase that is less apparent for $\Delta_c = 200$. On the contrary, the AGN simulation produces fewer halos of fixed mass than the DM one. Due to limited simulation box size, only a few halos have mass $M \geq 10^{15} h^{-1} M_\odot$ for FoF and SO with $\Delta_c = 200$. Given the limited dynamical range accessible to our simulations, we attempt in the following to provide fitting expressions to the corrections to the HMF induced by baryon effects, while we avoid providing absolute fitting functions to the HMF.

4.1 The HMF from Friend-of-Friend

We compare in the upper panel of Fig. 1 the HMFs for the three different simulations, while the lower panel shows the relative difference between each of the two hydrodynamical simulations and the DM one. As for the effect of the baryon physics described by the CSF model, we note that the difference with respect to the DM case has a clear redshift evolution and halo mass dependence. As redshift decreases from $z = 2.2$ to 0, the HMF ratio drops from ~ 1.6 to ~ 1.1 , with a weak increasing trend of this ratio with halo mass, at all redshifts. Quite remarkably, including AGN feedback has the effect of reducing the difference with respect to the DM-only case: the HMF ratio drops to about unity for massive halos with $M_{\text{FoF}} \gtrsim 10^{14} h^{-1} M_\odot$, while at smaller halo mass it decreases to ~ 0.9 for $M_{\text{FoF}} \approx 10^{13} h^{-1} M_\odot$. Unlike the CSF case, these differences do not show any evidence of redshift evolution from $z = 1$ to $z = 0.0$. At higher redshift, $z = 2.2$, the HMF ratio keeps fluctuating around 1, as a consequence of the limited statistics of halos due to the finite box size.

4.2 The HMF from Spherical Overdensity

We compare in the upper panels of Fig. 2 the HMFs obtained from the SO halo finder at three overdensities, $\Delta_c = 2500, 500, 200$ (from left to right), along with the ratios of

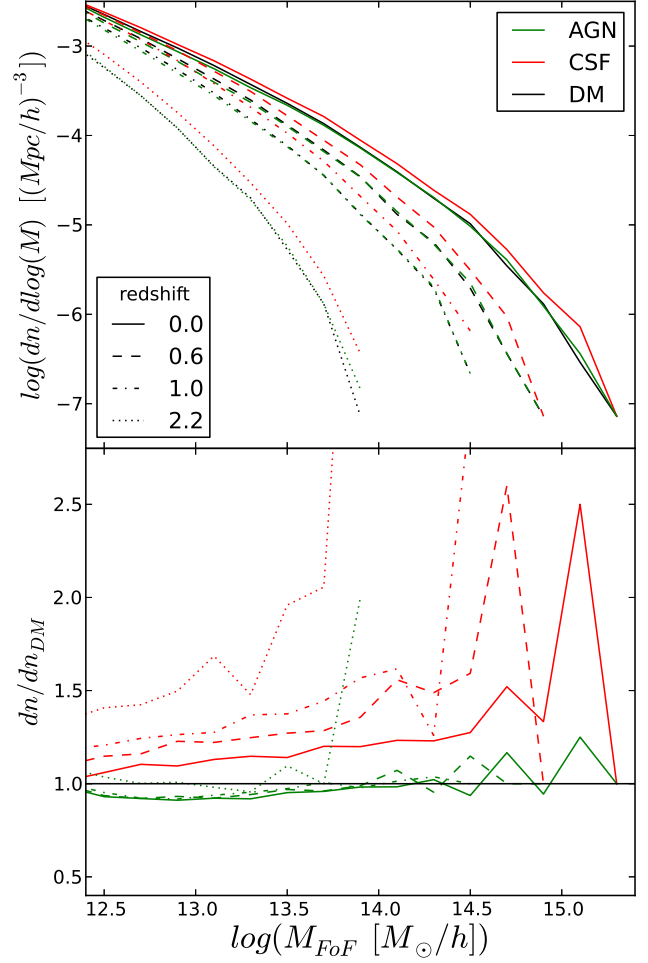


Figure 1. Baryon effects on the halo mass function (HMF) for halos identified with the Friend-of-Friends (FoF) algorithm. Upper panel: FoF halo mass functions (HMFs). Different line styles are for different redshifts, as indicated in the legend in the bottom left corner, while different colours refer to the different simulations (legend in upper right corner). Lower panel: ratios between each of the HMFs from the hydrodynamical simulations and the HMF of the DM simulation.

the HMFs from the CSF and AGN simulations with respect to the DM-only result (lower panels). As expected, baryons have a larger impact at the highest considered overdensity, $\Delta_c = 2500$. In this case, the ratio between CSF and DM HMFs shows a redshift evolution similar to the FoF results but with a higher amplitude, ranging from ~ 1.4 at $z = 0$ to ~ 2.5 at $z = 2.2$, but with no significant dependence on the halo mass. At lower overdensities, $\Delta_c = 200$ and 500 , the redshift evolution becomes weaker and the differences with respect to the DM case are reduced, with only a $\lesssim 5$ per cent difference at $\Delta_c = 200$ (similar results for the CSF case were also found by Paper I).

When AGN feedback is included in the simulation, the corresponding HMF drops below the HMF from the DM simulation, by an amount that decreases for lower Δ_c values, with no evidence for redshift dependence of the HMF difference. At $\Delta_c = 2500$, this ratio has a weak halo mass dependence, ranging from ~ 0.7 at $10^{12.5} h^{-1} M_\odot$ to ~ 0.5 at

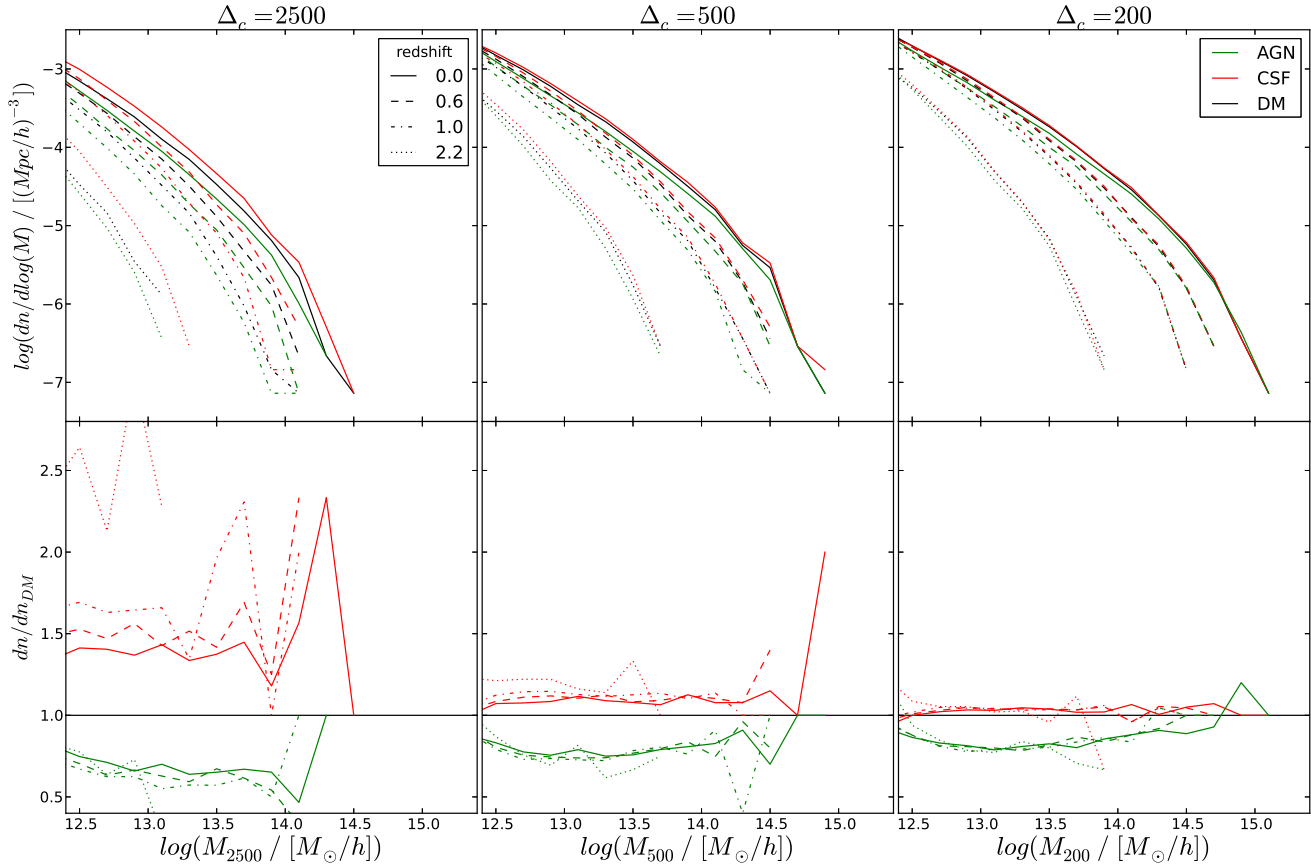


Figure 2. Effect of baryons on the halo mass function (HMF) for spherical overdensity (SO) halos. Each panel is the same as in Fig. 1, but for the spherical SO HMFs with halo masses computed for $\Delta_c = 2500$ (left panel), 500 (middle panel) and 200 (right panel).

$10^{14} h^{-1} M_\odot$. At $\Delta_c = 500$ and 200, the difference between AGN and DM HMFs reduces, with a mild dependence on halo mass: $dn/dn_{DM} \approx 0.7, \approx 0.8$ at $M \approx 10^{13} h^{-1} M_\odot$ to $dn/dn_{DM} \approx 0.9, \approx 1.0$ ($\Delta_c = 500, 200$, respectively) in the high mass end.

In general, the effect of including baryons on the HMF goes in the same direction, independent of whether FoF or SO halo finders are used. While this holds at a qualitative level, as expected quantitative differences between FoF and SO results are found, especially for the AGN case. As we will discuss in the following, the effect of including AGN feedback is that of producing halos that are less concentrated than in the CSF case. As a result, one expects that matching SO and FoF HMFs requires in the CSF simulation a higher Δ_c than in the AGN simulation. Many efforts are made to rematch the two halo mass functions by tuning b and Δ_c (for example Lukić et al. 2009; Courtin et al. 2011; More et al. 2011). However, as shown in Watson et al. (2013), even in dark-matter-only simulations, matching FoF HMFs to SO HMFs not only depends on the choice of b and Δ_c , but also on the concentration parameter, pseudo mass evolution, and the problems inside the two algorithms. These quantitative differences between FoF and SO results make this matching progress even more complex if baryon models are taken in account.

In order to understand the origin of the baryonic effects on the HMFs predicted by our simulations, we further

focus on the difference of masses of matched halos at overdensity $\Delta_c = 500$ (see Section 3.3 for the description of the matching procedure). We show in Fig. 3 the ratio between masses of matched halos in each one of the two hydrodynamical simulations and in the DM simulation (red and green points for the CSF and AGN case, respectively). In each panel, the thick lines show the mean value of these ratios computed within each mass bin (magenta for CSF and blue for AGN). As for the CSF case, the effect of baryons is that of increasing halo masses by an amount which is almost independent of redshift. At each redshift, the halo mass ratio weakly decreases with halo mass, from ~ 1.1 at $M_{500} = 10^{12.5} h^{-1} M_\odot$ to ~ 1.05 at $M_{500} \gtrsim 10^{13.5} h^{-1} M_\odot$, then becoming constant (see also Paper I). As for the AGN simulation, the effect of baryons goes in the opposite direction of decreasing halo masses, thereby decreasing the corresponding HMF, as shown in Fig. 2. Also in this case, there is no evidence for a redshift evolution of the halo mass ratio, at least below $z = 1.0$. However, there is an obvious increase of this ratio with halo mass, that ranges from ~ 0.8 at $M_{500} = 10^{12.5} h^{-1} M_\odot$ to $\simeq 1$ for the most massive halos found in our simulation box. Similar trends are also found for the mass ratio with $\Delta_c = 2500, 200$, both of which also show no evidence of redshift dependence for both hydrodynamical simulations. We verified that using the median value of those data points gives almost identical lines to these mean lines. As discussed in the Appendix C, this

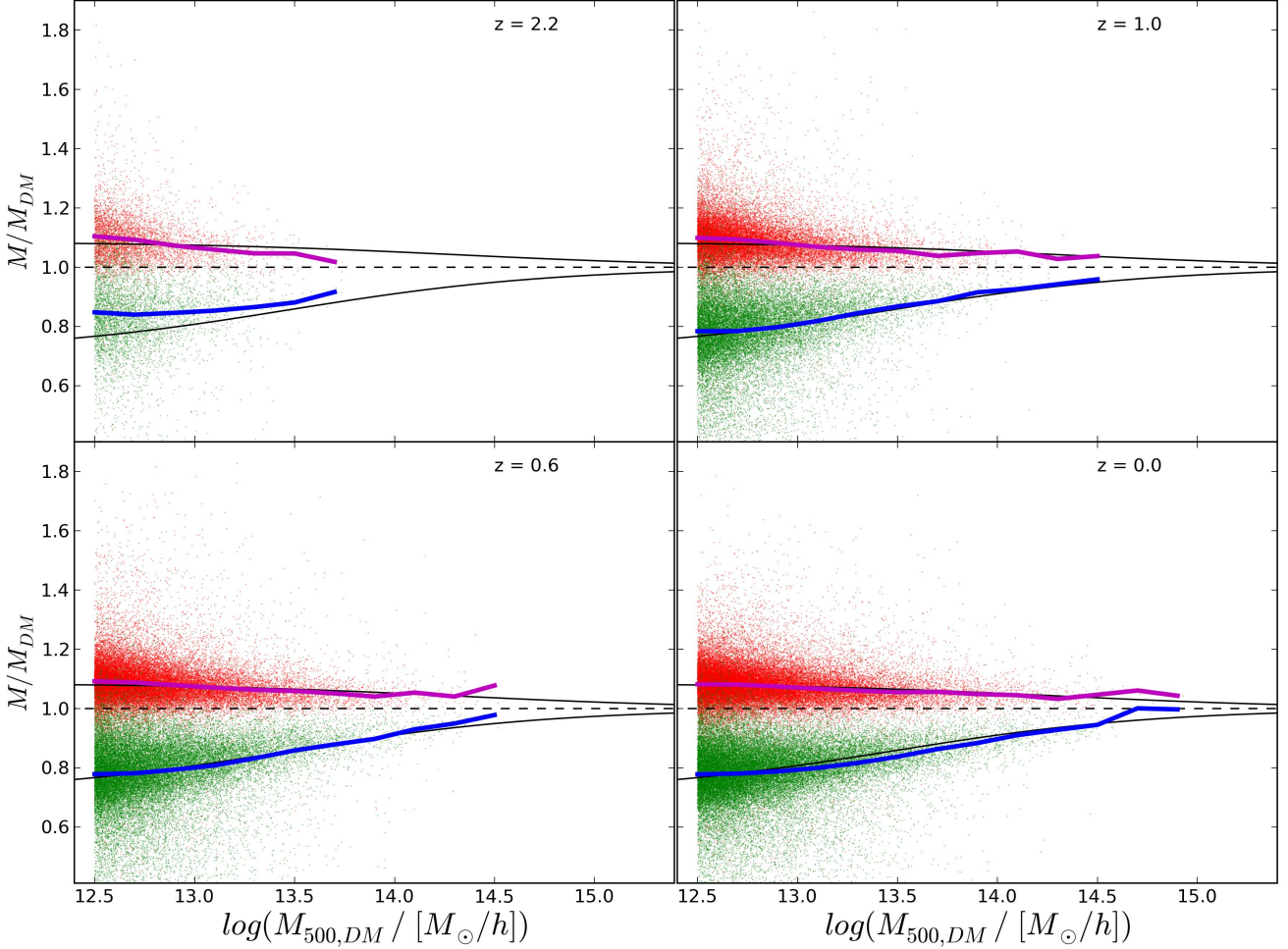


Figure 3. Mass dependence of the ratio of masses of matched SO halos computed for $\Delta_c = 500$ at different redshifts, as reported in the upper-right corner of each panel. Each point represents a halo mass ratio between the matched CSF (red points) or AGN (green points) halos to DM ones, as a function of the mass of the matched halo in the DM simulation. The thick magenta and green lines show the mean values of this ratio within each mass bin for the CSF and AGN simulations, respectively. The best-fitting relation for the mass correction of Eq. 1 is shown with the solid black lines. We note that the same relation provides a good fit at all redshifts, at least up to $z = 1$. See Table 1 for the values of the parameters defining this best-fit relation.

effect of reduction of halo masses in the presence of AGN feedback is quite robust against numerical resolution. We refer to this Appendix for a more detailed discussion of the resolution test that we carried out.

Since the masses of SO halos are computed by adding up all the particles within a sphere with radius R_{Δ_c} , it is clear that a change of the halo density profiles induced by the presence of baryons would also change the corresponding values of R_{Δ_c} . In order to quantify the effect of this variation, we also compute masses for each halo in the CSF/AGN simulations by using the value of R_{Δ_c} of the corresponding halo identified in the DM simulation. In Fig. 4, we show again the halo mass difference at $\Delta_c = 500$ after applying this re-tuning of the halo radii. A comparison with the $z = 0$ result from in Fig. 3 demonstrates that these ratios are only slightly shifted towards unity, for both CSF and AGN models. This small change implies that the differences in halo masses are mostly contributed by the baryon effects on the

halo density profiles, which can not be recovered by simply changing the halo radius.

Including only SN feedback in the form of galactic ejecta is already known not to be able to regulate overcooling at the centre of relatively massive halos, with $M > 10^{12.5} h^{-1} M_\odot$. Adiabatic contraction (e.g. Gnedin et al. 2004), associated to the condensation of an exceedingly large amount of cooled gas, leads then to an increase of density within a fixed halo aperture radius and, therefore, to an increase of the halo mass with respect to the DM case. The opposite effect is instead associated to the inclusion of AGN feedback. In this case, the sudden displacement of large amount of gas at epochs corresponding to the peak of AGN feedback efficiency, taking place at $z \sim 2-3$, causes sudden variations of the halo potential, which reacts with an expansion, thus decreasing halo masses (see discussion in Sect. below).

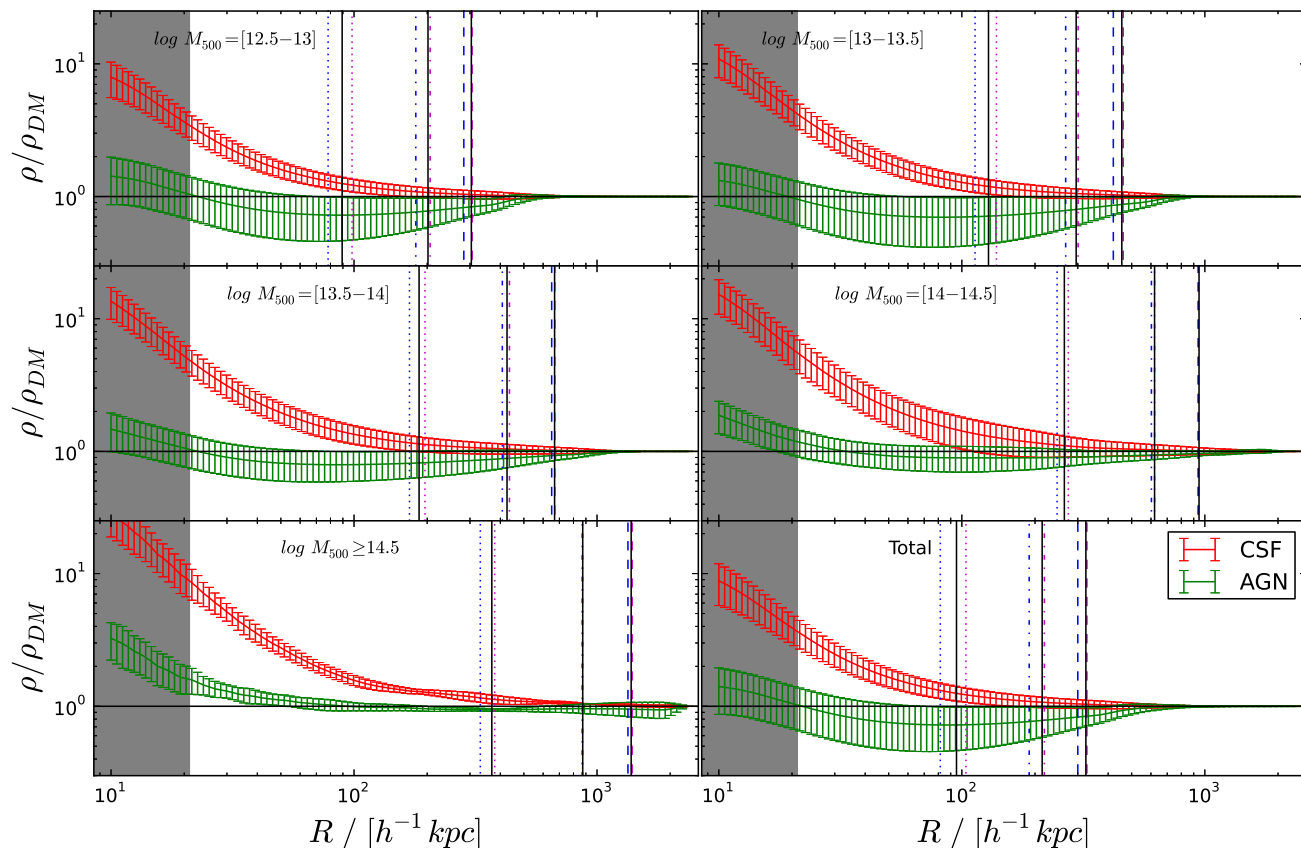


Figure 5. The stacked ratios of cumulative density profiles, $\rho(< R)$, of matched halos identified in each one of the hydrodynamical simulations and in the DM one. Different panels refer to different halo mass ranges, with the bottom right panel showing the results for all halos with mass $M_{500} \geq 10^{12.5} h^{-1} M_{\odot}$. In each panel, the red and green solid lines are for the mean density ratios for the CSF and AGN case, respectively. Error bars indicate the 1σ scatter around the mean. Vertical dashed, dot-dashed and dotted lines indicate the median values of R_{200} , R_{500} and R_{2500} computed within each halo mass interval, with magenta and blue colours referring to the CSF and AGN simulations, respectively. We also show with continuous black lines the median values of R_{2500} , R_{500} and R_{200} for the DM simulation. The shadow regions show the limits of the gravitational softening.

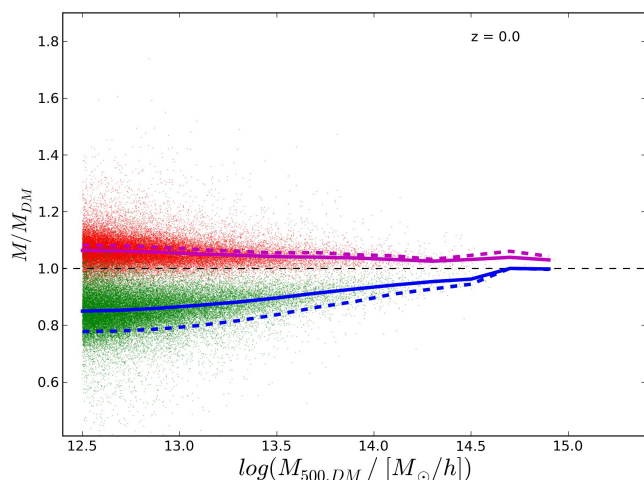


Figure 4. The same as the bottom right panel of Fig. 3, but for halo masses in the CSF/AGN simulations computed within the R_{500} radius of the corresponding halos from the DM simulation. The dashed thick lines are the previous results in Fig. 3 at $z = 0$.

4.3 Density profiles

Having quantified the variation of halo masses, we now discuss how this variation is associated to changes in the total density profiles of halos induced by baryonic processes.

To this purpose, we show in Fig. 5 the stacked ratio between density profiles for halos belonging to different mass intervals. We consider in this plot halos that are matched in the CSF/AGN and in the DM simulations. Halos are separated into five mass bins, according to the M_{500} halo mass, measured in the DM simulation. For each matched halo, we first compute the ratio of cumulative density profiles, $\rho(< R)$. Then, we stack the density profile ratios for all halos belonging to the same mass bin. The stacked density profile ratios for CSF and AGN halos are shown with red and green curves, respectively, with error bars indicating the 1σ intrinsic scatter within each mass interval.

We note that density profiles for CSF halos are always higher than those for the DM simulation for all mass bins. The effect is stronger towards the cluster centre, as a result of adiabatic contraction triggered by gas condensation from cooling. This result, which is in line with those found by several previous analyses (e.g. Gnedin et al. 2004;

	$\Delta_c = 2500$	$\Delta_c = 500$	$\Delta_c = 200$
AGN			
M_0	13.952	13.471	13.334
α	0.322	0.288	0.274
CSF			
M_0	13.629	14.305	14.182
α	0.295	0.085	0.045

Table 1. Values of the best-fitting parameters describing the variation of mass of matched halos in the AGN, CSF and in the DM simulation, as described by Eq. 1.

Puchwein et al. 2005), indicates that the feedback included in our CSF model is not efficient in counteracting the effect of radiative cooling in increasing total density in central halo regions. While the effect is quite small at R_{200} , it becomes sizeable at R_{2500} , where density increases by up to about 50 per cent for the smallest resolved halos.

It is quite interesting that a different behaviour is found when AGN feedback is included. In this case, an increase of total density associated to gas condensation is only found at small radii, below $(20\text{--}30) h^{-1}\text{kpc}$, which are however close the smallest scale that can be trusted at the resolution of our simulations. At larger radii the effect of AGN feedback is that of decreasing the halo density profile, an effect that becomes negligible at large radii, approaching R_{200} , and for the most massive halos found in our simulations. This result is in line with those from previous analyses of cluster simulations including AGN feedback (e.g. Duffy et al. 2010; Mead et al. 2010; Dubois et al. 2010; Killedar et al. 2012; Martizzi et al. 2013; Cui et al. 2014). The decrease of density profiles is caused by the effect of AGN feedback that, at redshifts corresponding to the peak of BH accretion $z \simeq 2\text{--}3$, causes a sudden expulsion of gas from the potential wells of the cluster progenitor halos (similar result is also found by Dubois et al. 2010). The expulsion of large amount of gas causes potential wells to react with some expansion, thereby causing a decrease of the density in central regions.

4.4 Correcting the halo mass function

Having traced the origin of the variation of halo masses induced by baryonic processes, we investigate now whether the application of a suitable correction to halo masses allows one to recover the HMF from a hydrodynamical simulation, starting from the DM-only HMF. In Paper I, we have already shown that the HMFs from non-radiative and CSF simulations can be corrected to the dark-matter-only HMF one, up to a residual scatter of $\lesssim 3$ per cent, by adopting a constant halo mass shift. From Fig. 3, we note that the mean values of the halo mass difference between AGN and DM simulations (thick blue line) has a significant mass dependence that needs to be included in the correction.

As a convenient relation to describe the mass-dependence of the mean mass ratio, we use these sigmoid

functions

$$\begin{cases} f(x) = \alpha/(1 + e^{-3(x-M_0)/2}) + 1 - \alpha & \text{AGN,} \\ f(x) = \alpha/(1 + e^{3(x-M_0)/2}) + 1 & \text{CSF,} \end{cases} \quad (1)$$

with M_0 and α considered as fitting parameters. Here, $f(x)$ is the halo mass ratio between AGN and DM sets, with $x = \log M_{\Delta_c, DM}$. Since the halo mass difference shows no evidence for redshift evolution, at least for $z \leq 1.0$, we do not attempt to fit a possible redshift dependence of the M_0 and α parameters and exclude the results at $z = 2.2$ from the analysis. The values of M_0 and α obtained in this way are reported in Table 1 for the three values of the overdensity Δ_c at which SO halos have been identified. The thin black line shown in Fig. 3 indicates this fitting to the correction for $\Delta_c = 500$. We verified that a redshift-independent mass correction also holds for the other Δ_c values up to redshift $z = 1$. Further, we also checked that the fitted parameters show no significant difference, whether we choose to use median mass ratio or the mean mass ratio.

We show in Fig. 6 the ratio between the HMFs from the CSF, AGN and from the DM simulations, after correcting halo masses in the former according to Eq. 1. In each panel, different line-types indicate results at different redshifts with different panels referring to different values of Δ_c . We note that the correction to halo masses allows one to recover the DM HMF to good accuracy, at least for masses larger than $10^{13} h^{-1} M_\odot$, the HMFs are matched to the DM one with no apparent systematic bias within random oscillations of $\lesssim 5$ per cent. We note that results become noisy whenever the sampling effects become important due to the limited halo statistics. This is the case for large masses and, especially, for the highest overdensity $\Delta_c = 2500$. At small masses, below $10^{13} h^{-1} M_\odot$, we note that the adopted mass correction systematically produces an overestimate of the corrected HMF for AGN set. For the smallest considered mass, $M_{DM} \geq 10^{12.5} h^{-1} M_\odot$, this overestimate is as large as 10–15 per cent, the exact value depending on the overdensity Δ_c . The reason for this lies in the fact that this fitting of Eq. 1 does not provide an accurate description of the mass correction at small halo masses due to the halo mass cut at $10^{12.5} h^{-1} M_\odot$, as also shown in Fig. 3.

5 DISCUSSION AND CONCLUSIONS

Based on a set of large-scale N-body and hydrodynamical simulations, we presented an analysis of the baryon effects on the halo mass function, with emphasis on the role played by gas accretion onto super-massive black holes (SMBHs) and the ensuing AGN feedback. As such, this analysis extends our previous one, presented in Paper I, to the case in which one accounts for a suitable model for AGN feedback that regulates star formation within massive halos, thereby improving the degree of realism of the simulated galaxy clusters and groups. We compared three simulations: a first one including only collisionless Dark Matter; a second one including hydrodynamics with radiative physics and supernova (SN) feedback; a third one which also includes AGN feedback. Based on these simulations, we analyse how the halo mass distribution reacts to overcooling and, in the presence of AGN feedback, to the sudden displacements and expulsion of large amount of gas.

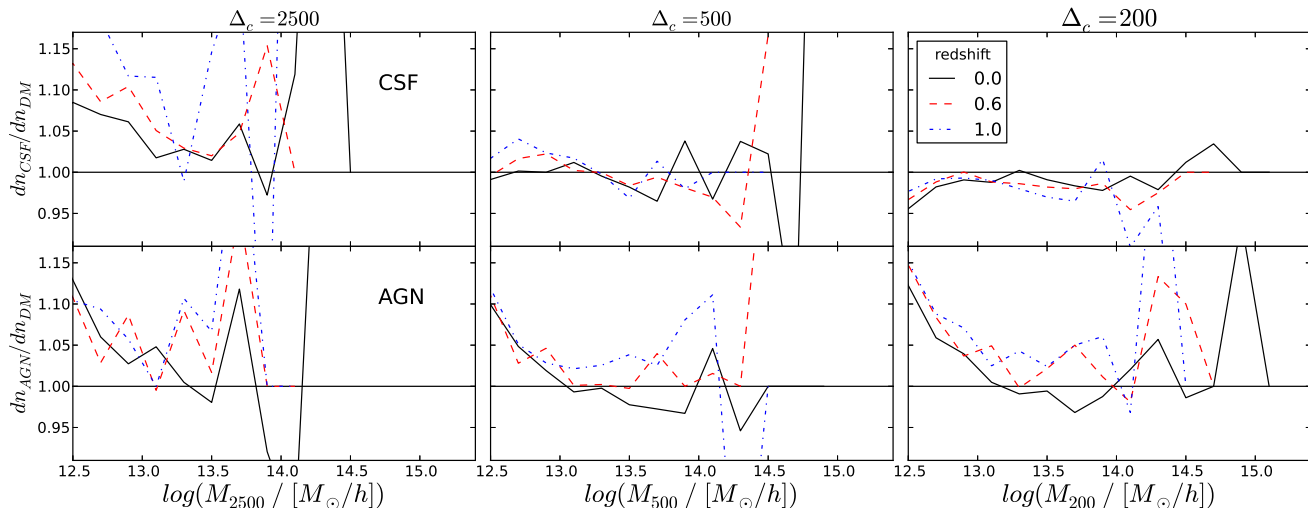


Figure 6. The ratios between the halo mass functions from the CSF (upper panel), AGN (lower panel) simulations and from the DM simulation, after applying the correction to DM halo masses, as described in the text. From left to right, we show results for overdensities $\Delta_c = 2500, 500, 200$. Different line styles and colors indicate different redshifts, as shown in the legend in the upper right panel.

We use both Friends-of-Friends (FoF) and Spherical Overdensity (SO) algorithms to identify halos. FoF halos are identified using a standard (on-the-fly) FoF finder with a linking length $b = 0.16$. As for SO halos, they are identified using an efficient memory-controlled python code — PIAO, in which halos are not allowed to overlap. We focus on three overdensities $\Delta_c = 2500, 500, 200$ for the SO halos.

The main results of our analysis are summarised as follows.

1. Including AGN feedback in hydrodynamical simulations causes a reduction of the halo mass function (HMF) with respect to the DM-only case, by an amount which depends on the overdensity within which halo mass is measured. This effect amounts to about 20 per cent for overdensity $\Delta_c = 500$, with no evidence of mass and redshift dependence, and increases at higher overdensity. Therefore, our model of AGN feedback reverses the effect of radiative physics with no efficient feedback, which instead leads to an increase of the HMF.

2. The baryonic effects on the HMF can be traced to the effect that different feedback models have on the halo density profiles and total masses. In the absence of AGN feedback, we confirm that halo density profiles steepen as a consequence of adiabatic contraction associated to overcooling, thus causing an increase of halo masses. AGN feedback generates shallower density profiles and a corresponding decrease of halo masses. This effect is caused by the improved regulation of overcooling associated to AGN feedback and to the sudden displacement of large amount of gas, which makes the gravitational potential responding with an expansion. The relative decrease of halo masses is larger in smaller objects, where AGN feedback is relatively more efficient, and at higher overdensities; for $\Delta_c = 500$, it amounts to ~ 20 per cent at $\log M_{500} = 12.5$, while becoming negligible for the largest halos found in our simulation box, with $\log M_{500} \simeq 15$. Interestingly, this effect is independent of

redshift, at least up to $z = 1$ where we have a large enough statistics of massive halos.

3. We provide a mass-dependent fit to the halo mass variations induced by baryonic effects. After applying this model for the mass correction to the HMF obtained from the DM-only simulation, we recover the HMF from hydrodynamical simulations, up to a random scatter of $\lesssim 5$ per cent for halos more massive than $10^{13} h^{-1} M_\odot$, with no significant bias and independently of redshift.

Our analysis demonstrates that baryon effects can cause sizeable variations of the HMF and, therefore, affects the measurement of cosmological parameters from redshift number counts of galaxy clusters. For instance, recent results from the Planck Collaboration (Planck Collaboration et al. 2013, cf. also Spergel et al. 2013) highlights that the cosmological model preferred by CMB analysis over-predicts the number of clusters expected in the SZ Planck Cluster Survey by about 50 per cent. Interestingly, this tension would be relaxed, although by a small amount, if the HMF calibrated with our AGN simulation is used to predict SZ cluster number counts.

In a recent paper, Khandai et al. (2014) also investigated the effect of including AGN feedback on the HMF. Since they considered simulation boxes smaller than our, with size of $100 h^{-1} M_\odot$, they better probed the low-mass end of the HMF, while having a worse sampling of the high mass end. As a result of their analysis, they found that the FoF halo mass function can be described with a universal form to a reasonable accuracy, even after accounting for baryon effects.²

² After the submission of our paper, a paper by Velliscig et al. (2014) appeared on the arXiv, which also included an analysis of baryon effects on halo masses and HMF, when AGN feedback is also included. Using box size and resolution quite similar to those of our simulations, they confirmed our results on the effect of AGN feedback on the HMF.

Numerical convergence in the calibration of the HMF from purely collisionless simulations could in principle be reached by “brute force” (i.e. increasing the dynamic range accessible and the gravitational force integration accuracy). The same may not be true when the effects of baryons are included. In fact, our analysis shows that baryons can generate variations of the HMF with respect to the DM case which goes in different directions, depending on the nature and, possibly, on the numerical implementation of feedback. In this respect, confidence in the calibration of baryon effects in the HMF is strictly related to the level of agreement between observational results and model predictions for a variety of properties of galaxy clusters. Current implementations of AGN feedback in cosmological simulations produce cluster populations with an increased degree of realism (e.g. Puchwein et al. 2008; Dubois et al. 2012; Planelles et al. 2013, 2014; Le Brun et al. 2013, and references therein). As an example, we compare in Appendix B two basic properties involving baryons in clusters, namely the stellar mass fraction and the total baryon mass fraction, with observational results. The good agreement between the AGN simulation and observational results is quite encouraging. Still, it is fair to admit that important tensions still exist between a number of observed and simulated cluster properties, such as the thermal structure of cool cores and the properties of the Brightest Cluster Galaxies (e.g. Dubois et al. 2011; Ragone-Figueroa et al. 2013; Planelles et al. 2014, cf. Kravtsov et al. (2014)). There is no doubt that providing an HMF, that accounts for the inclusion of the baryon physics at the percent level of accuracy required by the next generation of large-scale cluster surveys, still requires substantial work and, ultimately, a precise numerical description of galaxy formation in a cosmological framework.

ACKNOWLEDGEMENTS

We thank the anonymous referee for a careful reading of the manuscript and for useful comments, and Francisco Navarro-Villaescusa for his help in using Python and MPI4Py. All the figures in this paper are plotted using the python matplotlib package (Hunter 2007). Simulations have been carried out at the CINECA supercomputing Centre in Bologna, with CPU time assigned through ISCRA proposals and through an agreement with the University of Trieste. WC acknowledges a fellowship from the European Commission’s Framework Programme 7, through the Marie Curie Initial Training Network CosmoComp (PITN-GA-2009-238356), and the supports from ARC DPI30100117, from UWA Research Collaboration Awards and from the Survey Simulation Pipeline (SSimPL; <http://www.ssimpl.org/>). We acknowledge financial support from the PRIN-MIUR 2009AMXM79 Grant, from a PRIN-INAF/2012 Grant, from the PD51 INFN Grant and from the “Consorzio per la Fisica di Trieste”.

REFERENCES

- Allen S. W., Evrard A. E., Mantz A. B., 2011, *ARA&A*, 49, 409
- Anderhalden D., Diemand J., 2011, *MNRAS*, 414, 3166
- Andreon S., 2010, *MNRAS*, 407, 263
- Angulo R. E., Hahn O., Abel T., 2013, *MNRAS*, 434, 3337
- Angulo R. E., Springel V., White S. D. M., Jenkins A., Baugh C. M., Frenk C. S., 2012, *MNRAS*, 426, 2046
- Balaguera-Antolínez A., Porciani C., 2013, *JCAP*, 4, 22
- Baldi M., 2012, *MNRAS*, 422, 1028
- Bhattacharya S., Habib S., Heitmann K., Vikhlinin A., 2013, *ApJ*, 766, 32
- Bhattacharya S., Heitmann K., White M., Lukić Z., Wagner C., Habib S., 2011, *ApJ*, 732, 122
- Bonafede A., Dolag K., Stasyszyn F., Murante G., Borgani S., 2011, *MNRAS*, 418, 2234
- Booth C. M., Schaye J., 2009, *MNRAS*, 398, 53
- Borgani S., Dolag K., Murante G., Cheng L.-M., Springel V., Diaferio A., Moscardini L., Tormen G., Tornatore L., Tozzi P., 2006, *MNRAS*, 367, 1641
- Brandbyge J., Hannestad S., Haugbølle T., Wong Y. Y. Y., 2010, *JCAP*, 9, 14
- Casarini L., Bonometto S. A., Borgani S., Dolag K., Murante G., Mezzetti M., Tornatore L., La Vacca G., 2012, *A&A*, 542, A126
- Cohn J. D., White M., 2008, *MNRAS*, 385, 2025
- Costanzi M., Villaescusa-Navarro F., Viel M., Xia J.-Q., Borgani S., Castorina E., Sefusatti E., 2013, *JCAP*, 12, 12
- Courtin J., Rasera Y., Alimi J.-M., Corasaniti P.-S., Boucher V., Füzfa A., 2011, *MNRAS*, 410, 1911
- Crocce M., Fosalba P., Castander F. J., Gaztañaga E., 2010, *MNRAS*, 403, 1353
- Cui W., Baldi M., Borgani S., 2012, *MNRAS*, 424, 993
- Cui W., Borgani S., Dolag K., Murante G., Tornatore L., 2012, *MNRAS*, 423, 2279 (Paper I)
- Cui W., Murante G., Monaco P., Borgani S., Granato G. L., Killeddar M., De Lucia G., Presotto V., Dolag K., 2014, *MNRAS*, 437, 816
- Cusworth S. J., Kay S. T., Battye R. A., Thomas P. A., 2013, e-prints arXiv:1309.4094
- Davis M., Efstathiou G., Frenk C. S., White S. D. M., 1985, *ApJ*, 292, 371
- Dubois Y., Devriendt J., Slyz A., Teyssier R., 2010, *MNRAS*, 409, 985
- Dubois Y., Devriendt J., Teyssier R., Slyz A., 2011, *MNRAS*, 417, 1853
- Dubois Y., Pichon C., Haehnelt M., Kimm T., Slyz A., Devriendt J., Pogossyan D., 2012, *MNRAS*, 423, 3616
- Duffy A. R., Schaye J., Kay S. T., Dalla Vecchia C., Battye R. A., Booth C. M., 2010, *MNRAS*, 405, 2161
- Ettori S., Dolag K., Borgani S., Murante G., 2006, *MNRAS*, 365, 1021
- Fabjan D., Borgani S., Tornatore L., Saro A., Murante G., Dolag K., 2010, *MNRAS*, 401, 1670
- Giodini S., Pierini D., Finoguenov A., Pratt G. W., et al. 2009, *ApJ*, 703, 982
- Gnedin O. Y., Kravtsov A. V., Klypin A. A., Nagai D., 2004, *ApJ*, 616, 16
- Gonzalez A. H., Sivanandam S., Zabludoff A. I., Zaritsky D., 2013, e-prints arXiv:1309.3565
- Gonzalez A. H., Zaritsky D., Zabludoff A. I., 2007, *ApJ*, 666, 147
- Grossi M., Verde L., Carbone C., Dolag K., Branchini E., Iannuzzi F., Matarrese S., Moscardini L., 2009, *MNRAS*, 398, 321

- Guo Q., White S., Boylan-Kolchin M., De Lucia G., Kauffmann G., Lemson G., Li C., Springel V., Weinmann S., 2011, *MNRAS*, 413, 101
- Hunter J. D., 2007, *Computing In Science & Engineering*, 9, 90
- Ichiki K., Takada M., 2012, *Phys. Rev. D*, 85, 063521
- Jenkins A., Frenk C. S., White S. D. M., Colberg J. M., Cole S., Evrard A. E., Couchman H. M. P., Yoshida N., 2001, *MNRAS*, 321, 372
- Khandai N., Di Matteo T., Croft R., Wilkins S. M., Feng Y., Tucker E., DeGraf C., Liu M.-S., 2014, e-prints arXiv:1402.0888
- Killedar M., Borgani S., Meneghetti M., Dolag K., Fabjan D., Tornatore L., 2012, *MNRAS*, 427, 533
- Knebe A., Knollmann S. R., Muldrew S. I., et al., 2011, *MNRAS*, 415, 2293
- Knebe A., Pearce F. R., Lux H., Ascasibar Y., et al., 2013, *MNRAS*
- Kravtsov A., Vikhlinin A., Meshcheryakov A., 2014, e-prints arXiv:1401.7329
- Kravtsov A. V., Borgani S., 2012, *ARA&A*, 50, 353
- Lacey C., Cole S., 1994, *MNRAS*, 271, 676
- Lagana T. F., Martinet N., Durret F., Lima Neto G. B., Maughan B., Zhang Y.-Y., 2013, *A&A*, 555, A66
- Lagana T. F., Zhang Y.-Y., Reiprich T. H., Schneider P., 2011, *ApJ*, 743, 13
- Le Brun A. M. C., McCarthy I. G., Schaye J., Ponman T. J., 2013, e-prints arXiv:1312.5462
- Lin W. P., Jing Y. P., Mao S., Gao L., McCarthy I. G., 2006, *ApJ*, 651, 636
- Lin Y.-T., Mohr J. J., Stanford S. A., 2003, *ApJ*, 591, 749
- Lin Y.-T., Stanford S. A., Eisenhardt P. R. M., Vikhlinin A., Maughan B. J., Kravtsov A., 2012, *ApJ*, 745, L3
- Lukić Z., Heitmann K., Habib S., Bashinsky S., Ricker P. M., 2007, *ApJ*, 671, 1160
- Lukić Z., Reed D., Habib S., Heitmann K., 2009, *ApJ*, 692, 217
- Maneewongvatana S., Mount D. M., 1999, e-prints arXiv:cs/9901013
- Martizzi D., Mohammed I., Teyssier R., Moore B., 2013, e-prints arXiv:1307.6002
- McCarthy I. G., Schaye J., Bower R. G., Ponman T. J., Booth C. M., Dalla Vecchia C., Springel V., 2011, *MNRAS*, 412, 1965
- Mead J. M. G., King L. J., Sijacki D., Leonard A., Puchwein E., McCarthy I. G., 2010, *MNRAS*, 406, 434
- More S., Kravtsov A., Dalal N., Gottlöber S., 2011, e-prints arXiv:1103.0005
- Murante G., Monaco P., Giovalli M., Borgani S., Diaferio A., 2010, *MNRAS*, 405, 1491
- Murray S. G., Power C., Robotham A. S. G., 2013, *MNRAS*, 434, L61
- Pillepich A., Porciani C., Hahn O., 2010, *MNRAS*, 402, 191
- Planck Collaboration Ade P. A. R., Aghanim N., Armitage-Caplan C., Arnaud M., Ashdown M., Atrio-Barandela F., Aumont J., Baccigalupi C., Banday A. J., et al. 2013, e-prints arXiv:1303.5080
- Planelles S., Borgani S., Dolag K., Ettori S., Fabjan D., Murante G., Tornatore L., 2013, *MNRAS*, 431, 1487
- Planelles S., Borgani S., Fabjan D., Killedar M., Murante G., Granato G. L., Ragone-Figueroa C., Dolag K., 2014, *MNRAS*, 438, 195
- Puchwein E., Baldi M., Springel V., 2013, *MNRAS*, 436, 348
- Puchwein E., Bartelmann M., Dolag K., Meneghetti M., 2005, *A&A*, 442, 405
- Puchwein E., Sijacki D., Springel V., 2008, *ApJ*, 687, L53
- Puchwein E., Springel V., Sijacki D., Dolag K., 2010, *MNRAS*, 406, 936
- Ragone-Figueroa C., Granato G. L., Murante G., Borgani S., Cui W., 2013, *MNRAS*, 436, 1750
- Rasia E., Borgani S., Ettori S., Mazzotta P., Meneghetti M., 2013, *ApJ*, 776, 39
- Reed D., Gardner J., Quinn T., Stadel J., Fardal M., Lake G., Governato F., 2003, *MNRAS*, 346, 565
- Reed D. S., Bower R., Frenk C. S., Jenkins A., Theuns T., 2007, *MNRAS*, 374, 2
- Reed D. S., Smith R. E., Potter D., Schneider A., Stadel J., Moore B., 2013, *MNRAS*, 431, 1866
- Rosati P., Borgani S., Norman C., 2002, *ARA&A*, 40, 539
- Rudd D. H., Zentner A. R., Kravtsov A. V., 2008, *ApJ*, 672, 19
- Sawala T., Frenk C. S., Crain R. A., Jenkins A., Schaye J., Theuns T., Zavala J., 2013, *MNRAS*, 431, 1366
- Schmidt F., Lima M., Oyaizu H., Hu W., 2009, *Phys. Rev. D*, 79, 083518
- Schneider A., Smith R. E., Reed D., 2013, *MNRAS*, 433, 1573
- Short C. J., Thomas P. A., Young O. E., Pearce F. R., Jenkins A., Muanwong O., 2010, *MNRAS*, 408, 2213
- Spergel D., Flauger R., Hlozek R., 2013, e-prints arXiv:1312.3313
- Springel V., 2005, *MNRAS*, 364, 1105
- Springel V., Di Matteo T., Hernquist L., 2005a, *ApJ*, 620, L79
- Springel V., Di Matteo T., Hernquist L., 2005b, *MNRAS*, 361, 776
- Springel V., Hernquist L., 2003, *MNRAS*, 339, 289
- Stanek R., Rudd D., Evrard A. E., 2009, *MNRAS*, 394, L11
- Sutherland R. S., Dopita M. A., 1993, *ApJS*, 88, 253
- Tinker J., Kravtsov A. V., Klypin A., Abazajian K., Warren M., Yepes G., Gottlöber S., Holz D. E., 2008, *ApJ*, 688, 709
- Tornatore L., Borgani S., Dolag K., Matteucci F., 2007, *MNRAS*, 382, 1050
- Tornatore L., Borgani S., Viel M., Springel V., 2010, *MNRAS*, 402, 1911
- van Daalen M. P., Schaye J., Booth C. M., Dalla Vecchia C., 2011, *MNRAS*, 415, 3649
- van Daalen M. P., Schaye J., McCarthy I. G., Booth C. M., Dalla Vecchia C., 2013, e-prints arXiv:1310.7571
- Velliscig M., van Daalen M. P., Schaye J., McCarthy I. G., Cacciato M., Le Brun A. M. C., Dalla Vecchia C., 2014, e-prints arXiv:1402.4461
- Warren M. S., Abazajian K., Holz D. E., Teodoro L., 2006, *ApJ*, 646, 881
- Watson W. A., Iliev I. T., D'Aloisio A., Knebe A., Shapiro P. R., Yepes G., 2013, *MNRAS*, 433, 1230
- White M., 2001, *A&A*, 367, 27
- White M., 2002, *ApJS*, 143, 241
- Wu H.-Y., Huterer D., 2013, *MNRAS*, 434, 2556
- Wu H.-Y., Zentner A. R., Wechsler R. H., 2010, *ApJ*, 713, 856

Zhang Y., Zhang P., Yang X., Cui W., 2013, Phys. Rev. D, 87, 023521

Zhang Y.-Y., Laganá T. F., Pierini D., Puchwein E., Schneider P., Reiprich T. H., 2011, A&A, 535, A78

Zhu X.-J., Pan J., 2012, Research in Astronomy and Astrophysics, 12, 1603

APPENDIX A: PIAO

In this Appendix, we present a simple strategy to overcome a possible memory limitation problem that can occur when dealing with high-resolution, large-volume simulations. We then incorporate this strategy in a standard Spherical Overdensity (SO) halo finder algorithm and describe our Python `spherIcAl` Overdensity code — PIAO³. We check the consistency of PIAO and tackle the problem of halo overlapping in SO methods in subsection A2. Finally, we also show that PIAO is very efficient in memory control.

A1 Methodology and program

With the rapid growth of supercomputing power, cosmological simulations increase not only in resolution, but also in sheer volume. Thus, the output dimension of these simulations increases enormously, up to several Terabytes, or even Petabytes. Analysing such a huge amount of data on a relatively small server, easily meets a memory shortage problem. Limited memory forbids reading all the simulation information at one time.

We use a simple strategy to overcome this problem: splitting the whole simulation box into small mesh-boxes, then analyzing them one-by-one. We apply this strategy in two steps. Step one: the whole box is meshed into small ones. Each mesh-box is written into separated files which only contain only the needed information. Step two: each file is iteratively read in and analysed. Although this strategy inevitable wastes time on IO processes and hard disk space, we show below that this meshing/IO time is usually very short compared to the time spent in actually performing the analysis.

We apply such a strategy to the SO method, and for this purpose we wrote a python code — PIAO. PIAO makes extensive use of the NumPy library. We also made a modification of the `cKDTree` package in the `sciPy.spatial` library, adding the SPH density calculation in it. We adopt the same SPH kernel as the GADGET code. To achieve high performance, `cKDTree` implements the algorithm described in Maneewongvatana & Mount (1999) in Cython. PIAO is also parallel with a python MPI package (MPI4py) to speed up the calculation by taking advantage of multi-core CPUs. In its first step, PIAO reads in particles' positions from simulation snapshots part by part, and meshes them into small boxes according to mesh size. Only particles' ID, position, and mass are saved into mesh files. In a second step, PIAO reads in one mesh file at a time, and builds a buffer region around this mesh-box by reading in information from all nearby mesh-boxes. All the particles' densities within the mesh-box and its buffer region are calculated using the

nearest neighbours N_{nbs} of each particle and applying the selected SPH kernel over them.

PIAO uses the following simple loop to identify SO halos:

- 1 The particle with the highest SPH density is chosen as the center of a SO halo.

- 2 The code iteratively finds a radius R_Δ , centered on the above particle, and enclosing a fixed overdensity $\Delta = M(< R_\Delta)/(4\pi/3R_\Delta^3)/\rho_{crit}$. If the center was within the current mesh-box, all properties of this halo are computed, and the halo is then saved.

- 3 All particles within the radius R_Δ are flagged and excluded from being new centers by themselves. If we do not allow halo overlapping, those particles are also excluded from belonging to further halos.

- 4 If the current halo contains less than a chosen number of particles N_{cut} , the cycle ends. All of the remaining particles will not belong to any halo.

- 5 Next particle with highest SPH density is selected, and the loop continues from step [2].

We paralleled PIAO using the MPI4Py package, to take advantage of multiple-core architectures. Since the analysis of each mesh-box is independent, this part is completely parallel and does not need any communication nor barrier. One processor is used for controlling and assigning tasks, i.e. mesh-cubes to free processes. This makes PIAO very flexible and balanced. In principle, it can run on any number of processors.

A2 Consistency Check

In this subsection, we test PIAO on a simulation, having 256^3 DM ($M_{DM} = 1.93 \times 10^7 h^{-1} M_\odot$) and 256^3 gas particles ($M_{gas} = 3.86 \times 10^6 h^{-1} M_\odot$) in a periodic box of comoving size $18h^{-1}$ Mpc. This simulation includes metal-dependent cooling, star formation, and SN thermal and kinetic feedback (see more details about the model for star formation and energy feedback in Murante et al. 2010). Also this simulation has been run using the TreePM-SPH GADGET-3 code with the same cosmological parameters of the simulations presented in the main text of the present work. We used this simulation instead of those described in Section 2 just because it contains a lower number of particles, and the analysis is thus quicker. Results on properties of galaxies and of diffuse baryons in that simulation will be presented elsewhere. Here we mainly focus on our halo finder performance, and in particular on two PIAO parameters: mesh-box size and SPH neighbour. We fix the overdensity parameter to $\Delta = 500$, and minimum number of particles per halo to $N_{cut} = 64$.

A2.1 Mesh-box size

Since PIAO employs a mesh to split the whole simulation into small boxes, we first need to check that such a splitting does not influence the halo identification procedure. We used two mesh-box sizes ($3, 6 h^{-1}$ Mpc) and checked our results against those obtained when the whole test simulation is analyzed without any splitting.

Given that the mesh-box size should not affect the results, we expect to find the same halo masses for the three

³ PIAO is publicly available at <https://github.com/ilaudy/PIAO>

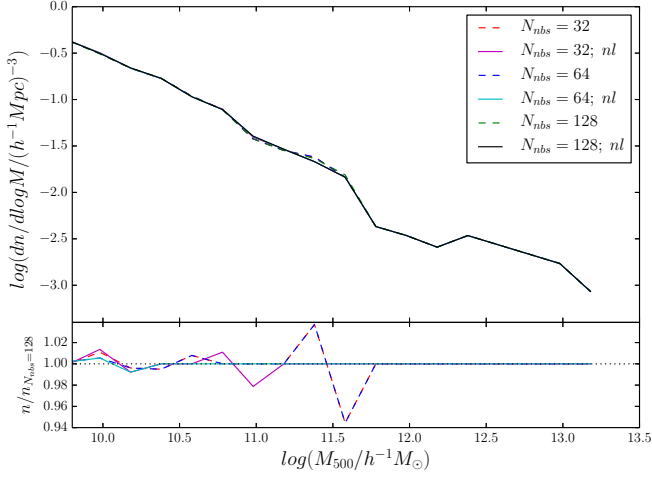


Figure A1. Halo mass functions at $\Delta = 500$ using different number of SPH neighbours (different line colors, see legend). Dashed lines represent halos identified allowing overlapping, while solid lines ones identified without any overlapping (“nl” in the legend). In the lower panel, ratios of the halo mass functions with respect with that obtained using $N_{nbs} = 128$ neighbours is shown (dashed lines for overlapping halos and solid lines for non-overlapping halos, respectively.)

different mesh-box sizes. Since we use the same SPH neighbours $N_{nbs} = 64$ for those tests, particles at the centers of identical halos are expected to have the same SPH density.

We decided that halos found in different analyses are the same one if their center particles have the same particle ID. All halos above mass $M_{500} = 1.5 \times 10^9 h^{-1} M_{\odot}$ are well matched between different mesh-box sizes. We confirm that all the matched halos have the same mass. Thus, mesh size does not change the properties of all identified halos. We found the same result both allowing and not allowing halos to overlap.

A2.2 SPH Neighbours

SPH density depends upon the number of neighbours N_{nbs} . Changing the SPH density of particles can change the identification of the most dense particle - i.e., the center of halo. If the center changes, all halo properties can also vary. We check the convergence of this parameter by using three SPH neighbours numbers $N_{nbs} = 32, 64, 128$ on our test simulation, keeping fixed the mesh-box size to $6 h^{-1} \text{Mpc}$.

In figure A1, we show halo mass functions from test simulation with different SPH neighbours. The meaning of the color and line-style is shown in the top-right legend. We show ratios of the halo mass functions with respect to that obtained using $N_{nbs} = 128$ in the lower panel. At the high mass end of the mass functions, $M_{500} \gtrsim 10^{12} h^{-1} M_{\odot}$, there are no differences between the results for any value of N_{nbs} . This means that this SPH neighbour parameter has no effect on massive halos. This SPH parameter makes the HMF ratio fluctuate below a halo mass of $\sim 10^{11.5} h^{-1} M_{\odot}$. While at smaller halo mass, these scatters are basically reduced within $\sim 1\%$. Above all, we expect that the SPH density accuracy will have a $\lesssim 3\%$ effect on halo mass function. If

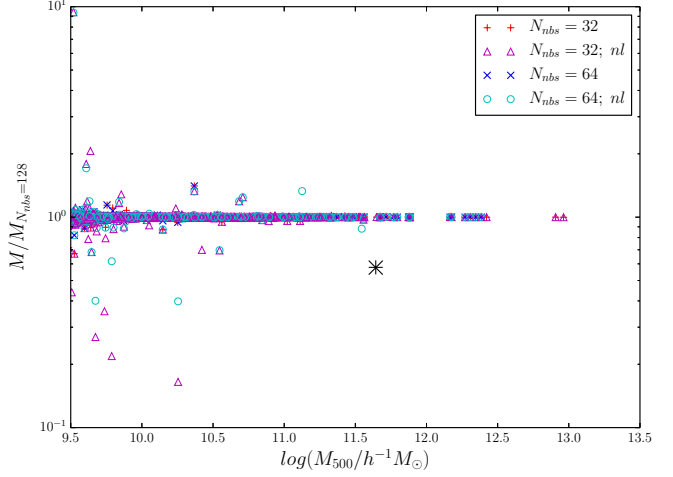


Figure A2. Ratio of halo mass function with respect to that obtained using halos identified with $N_{nbs} = 128$ SPH neighbours, as a function of halo mass M_{500} . As shown in legend, different color symbols indicate halos identified with a different number of SPH neighbours. As in Figure A1, “nl” in legend indicates non-overlapping halos. Big black symbols indicate that the matched halos have a center offset larger than $50 Kpc/h$.

we don’t allow halos to overlap, the discrepancies are even smaller.

We also matched all the individual halos having mass $M_{500} > 1.5 \times 10^9 h^{-1} M_{\odot}$ and found using $N_{nbs} = 128$ neighbours, with those identified using $N_{nbs} = 32$ and 64 neighbours. First, we matched halos with the central particle having the same ID. Then, for all unmatched halos from our $N_{nbs} = 128$ analysis we calculated the minimum distances from the centers of unmatched halos in the $N_{nbs} = 32, 64$ analyses. If such a distance is smaller than both the $N_{nbs} = 128$ and the $N_{nbs} = 32, 64$ halo radius, we decided that the corresponding halos matches. After this one-by-one matching procedure, we are left with 7 (0.15%) unmatched halos in our $N_{nbs} = 32$ analysis and 1 (0.02%) with the $N_{nbs} = 64$ one when we allow overlapping. In the case of non-overlapping halos, we have 5 (0.11%) unmatched objects for our $N_{nbs} = 32$ analysis and 2 (0.04%) for the $N_{nbs} = 64$ one. Most of the unmatched halos have $M_{500} < 10^{10} h^{-1} M_{\odot}$. We show the halo mass ratios in figure A2 for all matched halos.

Even if the halo number, at a given mass scale, changes less than 3 % (as discussed above), inaccuracies in the SPH density evaluation can lead to large halo mass difference for particular objects (see magenta triangles in figure A2). Therefore, when halo-by-halo matching is needed, we recommend a higher number of neighbours to be used in the density evaluation.

A2.3 Overlapping Problem

In X-ray or SZ observations, clusters are usually allowed to overlap, and overlapping objects count as separate objects. However, usually such observations only focus on most massive clusters, with masses larger than $10^{13} M_{\odot}$. Overlapping between these clusters is rare. Even if two halos with such a mass overlap, at worst one halo will have its mass increased

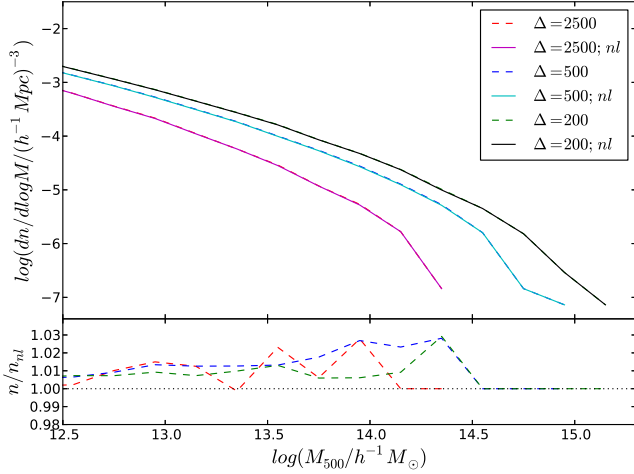


Figure A3. Halo mass functions at different overdensities $\Delta = 2500, 500, 200$. The meanings of line colors and styles are shown in the top-right legend. Lower panel shows the ratio between overlapping and non-overlapping halo mass functions. When we allow halos to overlap the mass function is over-predicted by $\lesssim 3\%$. This number has a weak dependence on halo mass. However, it seems consistent for the three overdensities.

of less than 50% with the other one suffering a equivalent mass decrease. Simulations span a wider mass range, currently five or more orders of magnitudes, and reach lower masses. We need to have an accurate halo mass function at per cent level over the whole covered mass range. Thus, the difference between overlapping and non-overlapping halo identification must be carefully examined.

To answer the question of how halo overlapping can change the halo mass function, we used PIAO to analyze our DM-only simulation described in section 2 at three overdensities $\Delta = 2500, 500, 200$, both allowing overlapping and not allowing it. Since SPH neighbours should not affect halo mass function too much (see the discussion in section A2.2), we fixed the number of SPH neighbours to $N_{nbs} = 64$. The minimum halo particle number parameter is set at $N_{cut} = 64$. Resulting halo mass functions are shown in figure A3. In the lower panel of this figure, we show the ratios of mass functions obtained at the various overdensities when we allow overlapping with respect to the non-overlapping case. The effect on the halo mass function is within 3 per cent over the whole halo mass range, with the overlapping case systematically overpredicting the mass function. This result does not strongly depend on the chosen overdensity nor on the mass scale, apart from the higher masses ($M > 10^{14.5} h^{-1} M_{\odot}$, where the two analyses give identical results).

A3 Summary

We used a simple meshing strategy to overcome the problem that analyzing large simulations on a small server or PC can be difficult due to memory limitation, and present a simple parallel Python spherical overdensity halo finding code — PIAO.

PIAO employs two additional parameters besides the overdensity Δ_c : the mesh-box size, which splits the whole

simulation box into smaller ones, and the SPH neighbours number, that is used for the SPH density calculation. In section A2, we showed that the mesh-box size parameter does not influence the identification of halos nor their properties. Since SPH density is used to locate halo density peaks, we further investigated the impact of the SPH neighbours number parameter on halo properties. The halo mass function is not strongly affected by it (at most at the $\lesssim 3\%$ level). On the other hand, one-by-one halo comparison suggests that an inaccurate density estimate may lead to large disagreements for individual halos. At last, we investigated the halo overlapping problem in section A2.3, and showed that the halo mass function is $\sim 1 - 3$ per cent higher for overlapping halos for three different overdensities, independently from the value of the overdensity.

We notice here, that all these tests in this appendix are done on a desktop PC, with a 4 core 2.67GHz CPU and total memory $\sim 3.4GB$. For test simulation with mesh-box size $6 h^{-1} \text{ Mpc}$ buffer region, peak using memory is $\lesssim 0.9GB$ for one processor. The meshing time is about 2 per cent of the analyzing time. For the DM simulation, we used mesh-box size $41 h^{-1} \text{ Mpc}$ and $4.5 h^{-1} \text{ Mpc}$ buffer region. Although the DM simulation has about 8 times more particles than the test simulation, the allocated memory for one CPU is only $\sim 10\%$ of the total memory, because the DM simulation was separated into 1000 mesh boxes. However, using the same number of CPUs, the analyzing time for the DM simulation is about 8 times more than for the test simulation.

APPENDIX B: THE STELLAR AND BARYON MASS FRACTION

For better understanding and calibrating the effects of baryons on the HMF, the baryon and stellar fraction can provide a key element. We define the total baryon mass fraction as the ratio between the gas+stars mass and the total mass within R_{500} : $f_b = (M_{gas} + M_{star})/M_{tot}$, while the stellar fraction is $f_s = M_{star}/M_{tot}$. The two fractions have been investigated in many works (from observation e.g. Lin et al. 2003, 2012; Gonzalez et al. 2007, 2013; Giodini et al. 2009; Andreon 2010; Zhang et al. 2011; Lagana et al. 2011, 2013), (or from theory e.g. Ettori et al. 2006; Borgani et al. 2006; Fabjan et al. 2010; Puchwein et al. 2010; McCarthy et al. 2011; Planelles et al. 2013; Le Brun et al. 2013). The total baryon fraction is commonly found to increase with the mass of the halo, while the stellar fraction seems to increase when going from clusters of galaxies mass scale to groups ones.

In Fig. B1, we show the baryon fraction f_b and stellar fraction f_s from CSF and AGN simulations, described in Section 2. The four panels show results from redshift $z = 2.2$ to $z = 0$. Different color points show the fractions f_b & f_s computed for the two simulations, for each halo, while the solid color lines are the mean of the points. Comparing the results from CSF and AGN sets, we can see that without AGN feedback, continuous star forming processes produce both higher stellar fraction f_s and baryon fraction f_b inside R_{500} compared to the AGN set at all redshifts. Similar to the finding of Planelles et al. (2013), both fractions, for the two simulations, show almost no redshift evolution for the most massive halos. However, at smaller halo mass, f_b computed on our CSF simulation shows a smaller decrease in time,

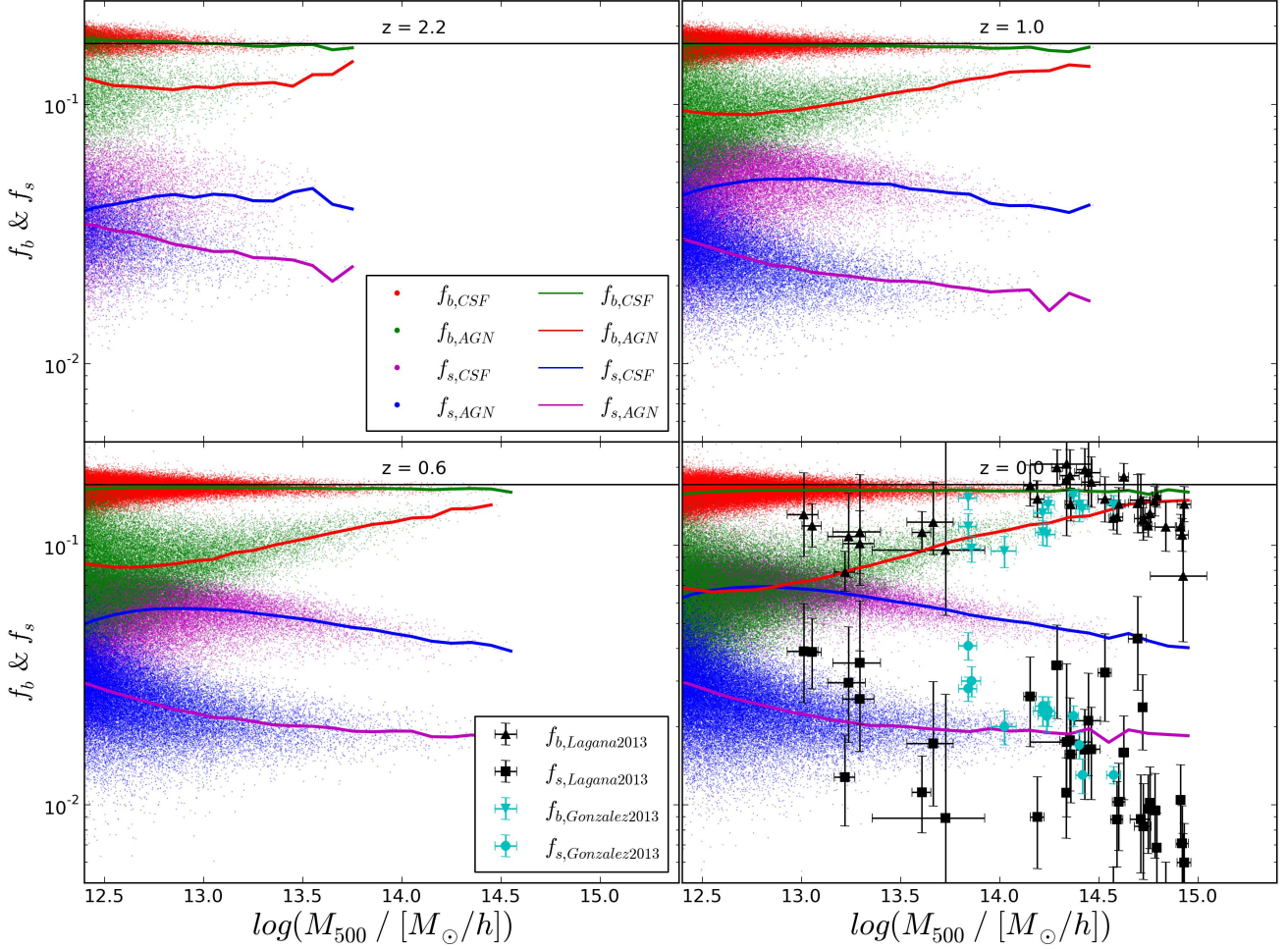


Figure B1. Baryon and stellar mass fraction within R_{500} for CSF and AGN simulations, described in Section 2. Different color points show baryon mass fraction (f_b) or stellar mass fraction (f_s) of each halo. Color lines are the mean value of the points. The line colors are reversed from points to highlight the difference, see the legend box in top-left panel for detail. The black horizontal line is the cosmic baryon mass fraction from our simulation. The three panels show the analysis at three different redshift $z = 2.2, z = 1.0$ and $z = 0.6$. In the lower-right panel, we compare the simulation results at redshift $z = 0.0$ to observations from (Lagana et al. 2013; Gonzalez et al. 2013) (see the legend in lower left panel).

when compared to the result from AGN simulation (~ 0.13 at $z = 2.2$ to ~ 0.07 at $z = 0$). The stellar fraction f_s computed on our CSF set increases with time, while there is a slightly decreasing trend for the same fraction calculated on our AGN simulation.

In the lower right panel of Fig. B1, we compare our results with observations from recent works of Gonzalez et al. (2013); Lagana et al. (2013) at redshift $z = 0$. Both papers use a WMAP 7 cosmology, and we corrected our results to account for that. Clearly, both fractions computed on our AGN simulation show a better match to the observations than our CSF simulation results. The trend of the fraction f_b with mass, in our AGN simulation, is also in good agreement with observations. However, the fraction f_s computed on the same AGN simulation is flatter than the observation results at the high mass end. This indicates that AGN feedback in our simulation is still not efficient enough to quench star formation at the observed levels in the most massive halos.

APPENDIX C: RESOLUTION TEST

In this section we discuss the convergence against numerical resolution of the results on the mass correction induced by the baryonic effects included in the AGN simulations. While we did not carry our simulations of cosmological boxes at higher resolution, we analyzed zoomed-in simulations of galaxy clusters and groups carried out at different resolutions. These simulations include all the baryonic effects as the AGN large-box simulation analyzed in this paper. More in detail, we used four of the 29 Lagrangian regions surrounding massive clusters, presented by Bonafede et al. (2011). Ragone-Figueroa et al. (2013) and Planelles et al. (2014), and presented results from hydrodynamical simulations of these Lagrangian regions which include the effect as SN and AGN feedback, as in the simulation considered in this paper. DM and baryonic particles in these simulations have masses of $8.47 \times 10^8 h^{-1} M_\odot$ and $1.53 \times 10^8 h^{-1} M_\odot$, respectively. As such they have mass resolution which is a factor of about four better than the cosmological simu-

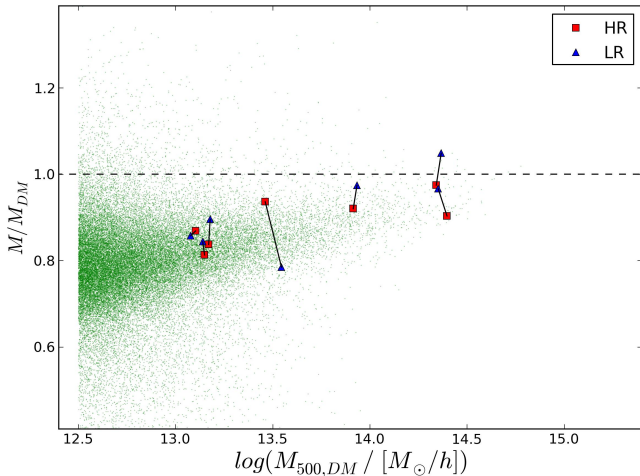


Figure C1. Resolution test at $z = 0$ for the values of the M_{500} halo masses. Small green dots are for the halos identified in the simulations analyzed in this paper (see also bottom right panel of Fig. 3). Overplotted are the results from zoomed-in simulation of galaxy clusters carried out for the DM and AGN cases, at two different resolutions. The lower resolution (LR; blue triangles) simulations have a mass resolution which is a factor of about 4 better than for the reference cosmological boxes, while the higher resolution (HR; red squares) have a mass resolution 10 times better than the LR ones. Cluster counterparts identified in the two simulations sets are connected by black solid lines.

lations presented in this paper. Four of these Lagrangian regions have been resimulated by further increasing mass resolution by a factor of 10. We identified 7 halos in these four simulations, all having masses of at least $10^{13} h^{-1} M_{\odot}$, whose counterparts in the low-resolution (LR) and high-resolution (HR) versions are both free of contaminant DM particles coming from outside the zoomed-in Lagrangian regions. The M_{500} values for these halos have been compared to the corresponding masses measured in DM-only version of the same simulations. The results on the mass variation induced by the baryonic effects included in the AGN simulations are shown in Figure C1, both for the LR and HR versions. Therefore, this figure illustrates how baryonic effects impact on halo masses when mass resolution is increased by a factor of about 40.

Clearly, the relatively small number of objects prevents us from drawing any robust statistical conclusion from this test. Still, we confirm the decrease of halo masses when AGN feedback is included. This decrease is also confirmed to be more pronounced in smaller halos, with a trend that shows no evidence of resolution dependence. This result is in line with the resolution test presented by Velliscig et al. (2014). More in detail, we note that the absolute value of halo masses in the DM-only simulations (as reported on the abscissa) can have small, but sizeable, variations with resolution, again with no obvious trend. The reason for these variations lies in the fact that, when mass resolution is increased, higher frequency modes from the linear power spectrum are also added when computing the displacement and velocity fields in the initial conditions. This effectively causing small variations in the timing of halo formations and

mergers, which result in variations of halo masses at a fixed redshift.

This paper has been typeset from a \LaTeX file prepared by the author.